ACS OMEGA

Open Access

http://pubs.acs.org/journal/acsodf

Article

Unraveling the Anion Storage Properties of Manganese-Doped $SrTiO_3$

Dushyant K. Sharma, Susanta S. Roy,* and Binson Babu*

Cite This: *ACS Omega* 2024, 9, 47332−47341

Read Online

ACCESS | Metrics & More | Article Recommendations | Supporting Information

ABSTRACT: Strontium titanate (STO), a cubic perovskite material, has gained recent attention as a supercapacitor active material with its pseudocapacitive energy storage attributed to anion intercalation. However, very few in-depth studies have been conducted to understand the anion storage properties of STO and its metal-doped derivative compounds. In this study, we explored the anion-insertion storage mechanism of Mn-doped strontium titanate (Mn-STO) compared to pristine STO. The polycrystalline Mn-STO, synthesized via solid-state reaction, showed 3-fold times higher electrochemical surface area and exhibited enhanced anion storage compared to pristine STO. Detailed anion kinetics and diffusion studies reveal that the anion storage in Mn-STO is dominated by the bulk diffusion-controlled pseudocapacitive process than in STO. Further, the supercapacitor fabricated with Mn-STO in a 3 M KOH aqueous electrolyte with 0.1 M $MnSO_4$ additives demonstrated excellent cycling stability, retaining 100% capacitance after 10,000 cycles, highlighting the potential of Mn-STO as an electrode material for supercapacitor applications.

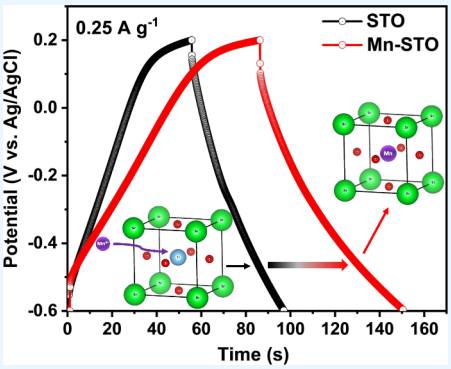

1. INTRODUCTION

Perovskite materials, having the formula of ABO_3, where A is the alkali earth metals/lanthanoids and B is the transition metal, have recently received greater attention for energy storage applications due to their unique structural and chemical compositions.[1−8] Moreover, it provides the possibility to tune the physical and electrochemical properties of the material by substituting multivalent ions at both A and B sites.[9−13] Further, the inherent oxygen vacancies and ionic conductivity of the perovskites show the potential of storing anions over cations.[14−16] Even though electrochemical oxygen intercalation was discovered in perovskites way back in the 1990s,[14] a systematic study of oxygen intercalation was first conducted by Mefford et al. in nanostructured $LaMnO_3$[1] for fast energy storage application. Later, different perovskite oxides, including $LaNiO_3$,[17] $LaNiO_{3-\delta}$,[2] $CaTiO_3$,[3] $SrCo_{0.9}Nb_{0.1}O_{3-\delta}$,[18] etc., are found to be suitable for the application of supercapacitors by storing charge through the mechanism of oxygen anion intercalation.

Strontium titanate ($SrTiO_3$, STO) is another type of cubic-structured perovskite material, having a Goldschmidt tolerance factor "*t*" of 1, recently explored as a potential active material for supercapacitors, exhibiting pseudocapacitive energy storage nature, which is attributed to the oxygen intercalation mechanism.[19,20] Nevertheless, the wide band gap of STO (3.2 eV) creates highly insulating nature, which affects its electrochemical performance.[21,22] Metal doping on STO is one of the methods used to improve electrochemical performances due to the increased electronic conductivities, creating more oxygen vacancies and hence enhancing the electrochemical surface area.[23,24] Ni, Cr, etc., are some of the dopants that enhance the electrochemical properties of STO.[22,25] Cao et al.[20] synthesized flexible Ce-doped $SrTiO_3$ ($SrCe_xTi_{1-x}O_3$) nanofiber perovskite films (SCTO-*x*) through the electrospinning method coupled with low-temperature sintering technology, exhibiting a very high specific capacitance of 1809.4 F g^{-1} at a current density of 1.875 A g^{-1}. Recently, we have reported chromium doping on STO through the solid-state method, which displayed improved pseudocapacitive nature due to the oxygen anion intercalation, and the fabricated symmetrical supercapacitor in an aqueous alkaline electrolyte displays enhanced storage properties with excellent cycling stability.[22]

In the present work, for the first time, we are investigating the electrochemical properties of manganese-doped $SrTiO_3$ (Mn-STO) in an aqueous electrolyte for the application of supercapacitors. Due to the matching of the ionic radii of Mn^{4+} (0.053 nm) with Ti^{4+} (0.061 nm), it is possible to substitute Mn^{4+} with Ti^{4+} without creating much change in the crystal structure and tolerance factor (t = 1.041). Further, the multivalency of Mn^{4+} and the defects/oxygen vacancies created during doping can enhance the electrochemical performance.

Received: September 30, 2024
Revised: October 11, 2024
Accepted: October 18, 2024
Published: November 15, 2024

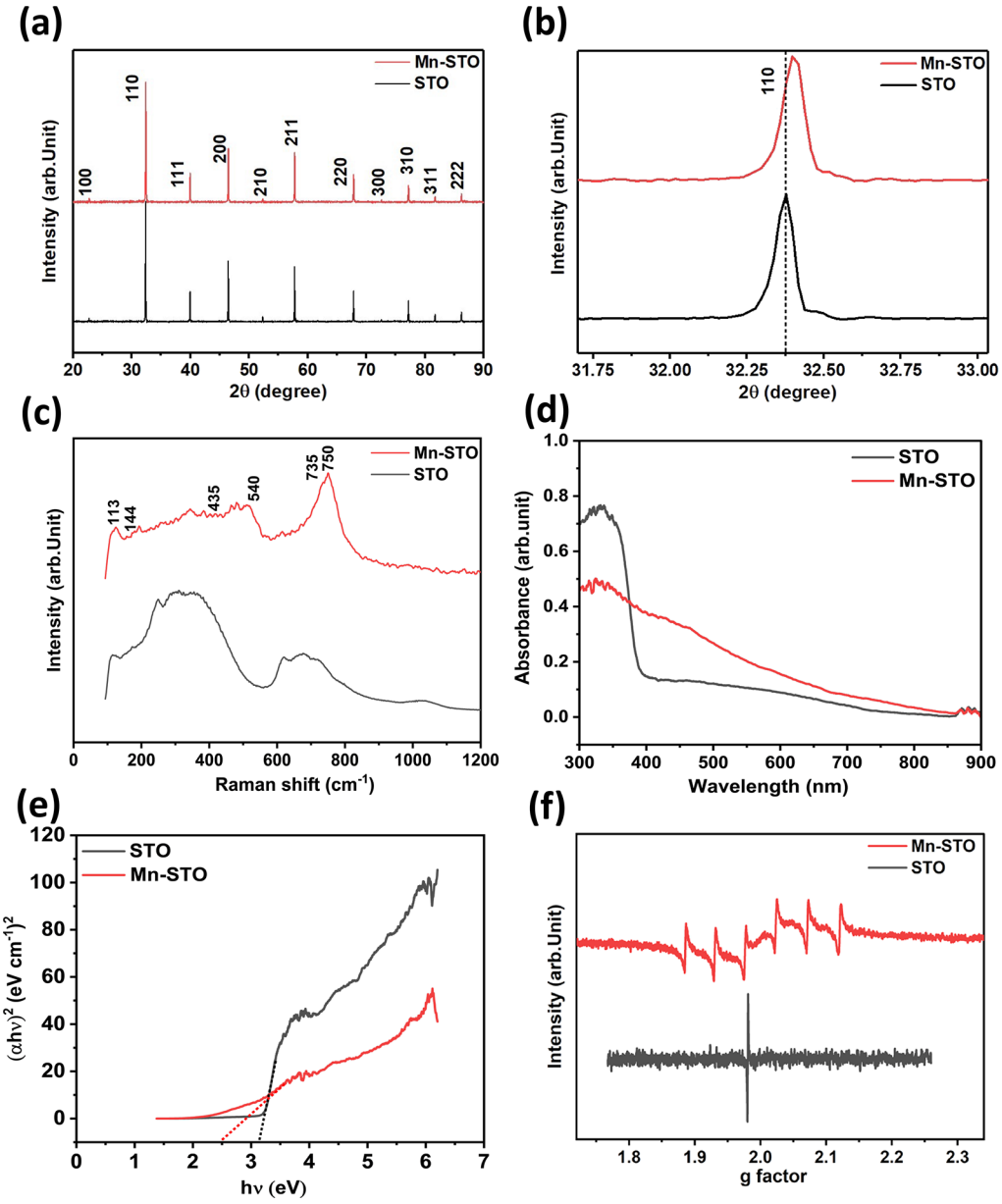

Figure 1. (a) Powder XRD pattern of the STO and Mn-STO samples. (b) Magnified view of the 110 plane showing a peak shift in Mn-STO. (c) Comparison of Raman spectra of STO and Mn-STO. (d) UV−visible spectra of STO and Mn-STO and (e) corresponding Tauc's plot to find the band gap. (f) EPR spectra of STO and Mn-STO.

Here, we are conducting a partial 5% Mn substitution through the solid-state method to synthesize Mn-STO (tolerance factor t = 1.001) and conducting various characterization techniques to elucidate the structural, morphological, and chemical compositions of the synthesized material. Detailed electrochemical characterizations of Mn-STO compared with STO are performed to evaluate the electrochemical performance, charge storage mechanisms, and kinetics. Further, the fabricated Mn-STO-based symmetric supercapacitor displays a good electrochemical performance with a high cycling stability of 100% capacitance retention over 10,000 cycles.

2. EXPERIMENTAL DETAILS

2.1. Preparation of STO and Mn-STO. The $SrTiO_3$ sample was synthesized via a solid-state reaction by mixing $SrCO_3$ (Alfa Aesar, 99.99%) with TiO_2 (Alfa Aesar, 99.99%) in a specific proportion. The mixture was then crushed and calcined at approximately 1050 °C for 12 h. Afterward, the resulting powder was manually ground and sintered at around 1350 °C for 24 h. After synthesizing $SrTiO_3$, 5% MnO_2 powder was added stoichiometrically, followed by calcination and sintering at 1050 and 1350 °C, respectively, producing 5% Mn-STO.

2.2. Material Characterization. The phase and crystal structure of the prepared samples were determined by using X-ray diffraction (Bruker D-8, K_α, λ = 1.5406 Å). Raman spectra and UV−vis optical spectra were recorded using an Andor Raman spectrometer 5.2 with a 532 nm laser source and a Shimadzu spectrophotometer (UV−vis 3700), respectively. Field emission scanning electron microscopy (FESEM) and energy dispersive X-ray analysis (EDX) (FESEM, JEOL7200) were employed to analyze the surface morphology as well as particle size and elemental composition of the samples, respectively. The morphology and polycrystalline nature of

https://doi.org/10.1021/acsomega.4c08911
ACS Omega 2024, 9, 47332−47341

the sample were confirmed by using transmission electron microscopy (TEM) (JEOL JEM2100 PLUS, 200 kV). Electron paramagnetic resonance (EPR) spectroscopy was carried out using a JEOL (X320, X band). The chemical state and composition of the samples were calculated by using X-ray photoelectron spectroscopy (XPS) (Thermo Fisher Scientific system at an operating voltage of 12,000 V).

2.3. Electrochemical Characterization. The electrodes were prepared by using the active material (STO and Mn-STO), activated carbon (Sigma-Aldrich, 99.99%), and poly-(vinyl difluoride) (pVdf) (Thermo Fisher Scientific (SDS), 99.99%), mixed at a mass ratio of 70:20:10, with *N*-methyl-2-pyrrolidone (Sigma-Aldrich 99.95%). The resulting slurry was uniformly coated onto a stainless steel disk current collector with a mass loading of ∼2.1 mg/cm^2. After coating, the electrode was dried in the vacuum oven at 120 °C for 12 h. The electrochemical surface area of the active materials was evaluated using a three-electrode configuration, with Ag/AgCl as the reference electrode and platinum wire as the counter electrode, in 5×10^{-3} M potassium ferro/ferricyanide in a 0.1 M KCl electrolyte. Further, the electrochemical storage properties of both electrodes were analyzed in the half-cell and full-cell configuration using a 3 M KOH alkaline aqueous electrolyte by using an Origalys multichannel electrochemical workstation and Neware BTS4000 (5 V, 20 mA). Various electrochemical characterizations, such as cyclic voltammetry, galvanostatic charge−discharge, and electrochemical impedance spectroscopy, were conducted to evaluate the performance of STO and Mn-STO.

3. RESULTS AND DISCUSSION

3.1. Material Characterization. The solid-state reaction method was employed to synthesize pristine STO and Mn-STO powders, as outlined in Section 3. The X-ray diffraction (XRD) measurements reveal the phase purity and crystal structure of the synthesized powder samples. The XRD pattern obtained for both synthesized STO and Mn-STO powders in a 2θ range of 20−90° (Figure 1a) indicates the phase pure single-phase cubic perovskite structure with a space group of *Pm*-3m (exactly matching with JCPDS file no. 350734).[22] The rightward shift of the 110-plane diffraction peak toward higher angles (Figure 1b), along with the reduction in the lattice constant and corresponding lattice volume, as determined from the Rietveld refinement of the XRD spectra (Figure S1a,b and Table S1), is attributed to the partial substitution of Mn^{4+} by Ti^{4+} at the B-sublattices in the ABO_3 perovskite structure of Mn-STO. This peak shifting and the lattice contraction are due to the smaller ionic radii of Mn^{4+} (∼0.53 Å) compared to Ti^{4+} (0.61 Å), respectively.[26−29]

Raman spectroscopy was utilized to probe the vibrational modes of the synthesized materials, which provides information regarding the local symmetries, crystallographic defects, and distortions at the molecular level.[30] Figure 1c shows the room-temperature Raman spectra of STO and Mn-STO. Pristine STO, which has an ideal cubic perovskite structure, displays two broad bands centered at ∼320 and 670 cm^{-1} as a result of the second-order Raman scattering process.[28,31−35] Since the pristine STO cubic perovskite structure has complete inversion symmetry, the first-order Raman scattering is not visible in agreement with the selection rules.[35] However, in Mn-STO, due to lattice distortion, local loss of inversion symmetry, and structure disorder, the previously Raman-forbidden modes in STO become active in Mn-STO, resulting in new modes at ∼113, 144, 435, and 540 cm^{-1}.[28,33,36,37] The presence of multiple cations (Mn^{4+}/Ti^{4+}) at the B-site of the ABO_3 crystal structure, where A represents the metal cation, B the transition metal, and O the oxide of Mn-STO, generates a sharp peak at ∼749 cm^{-1} along with two shoulder peaks at ∼735 cm^{-1} and ∼777 cm^{-1}. These are assigned to the A1g mode, representing the short-range ordering of ions at the B-site.[36,38−42]

The electronic transitions and the band gap of pristine STO and Mn-STO were investigated by employing UV−Vis optical spectroscopy. The absorption spectra of both materials display strong absorption in the UV region (Figure 1d). The flattening of the Mn-STO absorption curve compared to the sharp absorption peak in pristine STO (∼337 nm) indicates increased light absorption in the visible region due to predominant Mn^{4+} doping.[27] Further, the substitution of Mn^{4+} for Ti^{4+} narrows the band gap, which is estimated from Tauc's plot, where pristine STO shows a wide band gap of ∼3.2 eV, whereas Mn-STO shows a reduced gap of ∼2.5 eV only (Figure 1e). This narrower band gap indicates that Mn^{4+} occupies Ti^{4+} sites without affecting Sr^{2+} sites.[27,43] The substitution of Mn^{4+} in the Ti^{4+} octahedral site in Mn-STO is further confirmed by the sextet structure shown in the electron paramagnetic resonance (EPR) spectra (Figure 1f), which is due to the hyperfine splitting of 74 Oe at the Landé *g*-factor of 1.98.[44−47]

The morphology of the synthesized pristine STO and Mn-STO was characterized by using field emission scanning electron microscopy (FESEM). The FESEM images display agglomerated inhomogeneous particle distribution with arbitrary size and shape in both samples (Figure 2a,d).

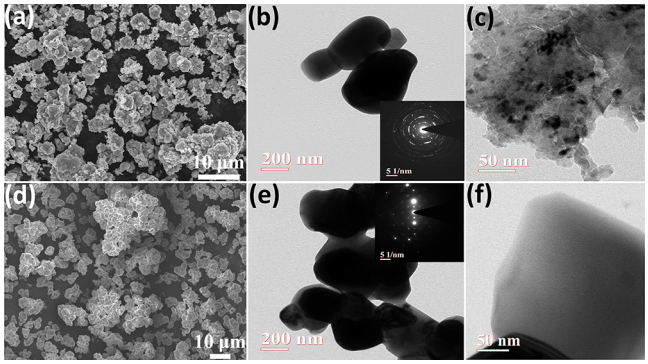

Figure 2. FESEM images of (a) STO and (d) Mn-STO. TEM images of (b, c) STO and (e, f) Mn-STO (inset figures display the SAED pattern of STO and Mn-STO).

Further, EDAX spectra and elemental mapping of both pristine STO and Mn-STO confirm the presence of Sr, Ti, and O elements, and the Mn incorporation is visible in Mn-STO (Figures S2 and S3 and Table S2). Transmission electron microscopy (TEM) displays the two-dimensional morphology of both samples (Figure 2b,c,e,f), further confirming the arbitrary particle size, and the selected area electron diffraction (SAED) pattern (insets of Figure 2b,e) reveals the polycrystalline nanocrystalline nature of both samples, which is corroborated by the XRD pattern (Figure 1a).

X-ray photoelectron spectroscopy (XPS) was used to investigate the chemical composition and oxidation state of the synthesized materials. The purity of both pristine STO and Mn-STO is further confirmed by the XPS survey scan (Figure

https://doi.org/10.1021/acsomega.4c08911
ACS Omega 2024, 9, 47332−47341

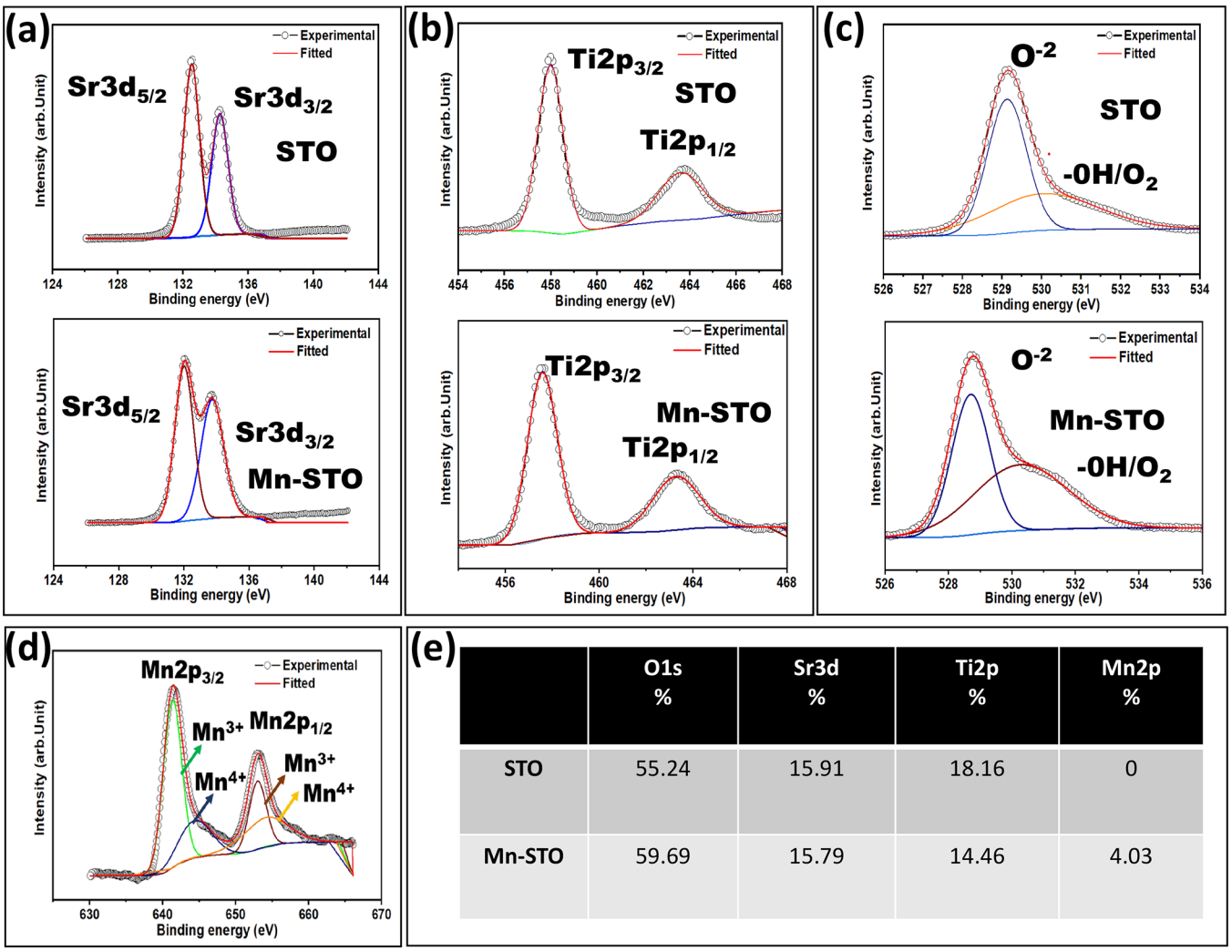

(e)

	O1s %	Sr3d %	Ti2p %	Mn2p %
STO	55.24	15.91	18.16	0
Mn-STO	59.69	15.79	14.46	4.03

Figure 3. High-resolution deconvoluted XPS spectra of (a) Sr 3d, (b)Ti 2p, (c) O 1s, and (d) Mn 2p in STO and Mn-STO and (e) corresponding atomic percentage of the elemental compositions.

S4). Figure 3 compares the high-resolution deconvoluted XPS spectra of Sr 3d, Ti 2p, O 1s, and Mn 2p in both materials, and their corresponding binding energy of different spin−orbit coupling states is shown in Table S3. The atomic weight percentage (Figure 3e) evaluated shows a Mn doping of ∼4.03% in Mn-STO, distorting ∼3.7% of Ti 2p[11] and ∼0.12% of Sr 3d, suggesting the predominant substitution of Mn^{4+} for Ti^{4+} over Mn^{2+} for Sr^{2+}. The deconvoluted spectra of Sr 3d (Figure 3a) illustrate the double split of the Sr^{2+} oxidation state into Sr $3d_{5/2}$ and Sr $3d_{3/2}$ peaks at the binding energies of 132.58 and 134.28 eV, respectively, with a peak difference of 1.7 eV.[48] However, in Mn-STO, a slight red-shift of ∼0.56 eV for Sr $3d_{5/2}$ (132.02 eV) and ∼0.53 (133.75 eV) for Sr $3d_{3/2}$ is observed, which is due to Mn incorporation in the STO lattice. Further, compared with the pure STO, a lower shifting of ∼0.41 and ∼0.33 eV is observed in the Ti $2p_{3/2}$ and Ti $2p_{1/2}$ split of Ti 2p, respectively, in the Mn-STO sample (Figure 3b). This indicates the formation of Ti^{3+} in the Mn-STO crystal lattices.[49] The deconvolution of high resolution of the O 1s peaks shows the presence of adsorbed $-OH/O_2$ molecules, which are found to be more in Mn-STO than in STO, as evidently shown from the split peaks centered at 530.27 and 530.04 eV, respectively (Figure 3c). This points out the possibility of formation of increased surface defects in Mn-STO as it can adsorb more $-OH/O_2$ species, which might bring higher electrochemical surface area compared to the pristine STO material.[50] Moreover, the presence of Mn^{3+} in Mn-STO, as evident from the respective Mn $2p_{3/2}$ (641.39 eV) and Mn $2p_{1/2}$ (653.06 eV) split peaks (Figure 3d), increases the conductivity of the material, which is also reflected in the band gap decrease investigated from the UV−visible absorption spectra in addition to the contribution of Mn^{4+} (Figure 1d,e).

3.2. Electrochemical Characterization. Cyclic voltammetry was utilized to investigate the electrochemical surface areas of both pristine STO and Mn-STO in a three-electrode setup, as described in Section 2. The electrochemical surface area, estimated from the Randel−Sevick equation,[51] shows a significant increase in Mn-STO (1.0358 mm^2) compared to pristine STO (0.3398 mm^2) (Figure S5). This enhancement is attributed to the defects created in STO during manganese doping, which is corroborated by XPS results indicating increased adsorption of $-OH/O_2$ species in Mn-STO. To evaluate the electrochemical performance of the synthesized materials, here, we utilized a 3 M KOH aqueous electrolyte solution. The rationale behind using an alkaline 3 M KOH aqueous electrolyte is evident from the high-area cyclic voltammogram exhibited by pristine STO compared to other

https://doi.org/10.1021/acsomega.4c08911
ACS Omega 2024, 9, 47332−47341

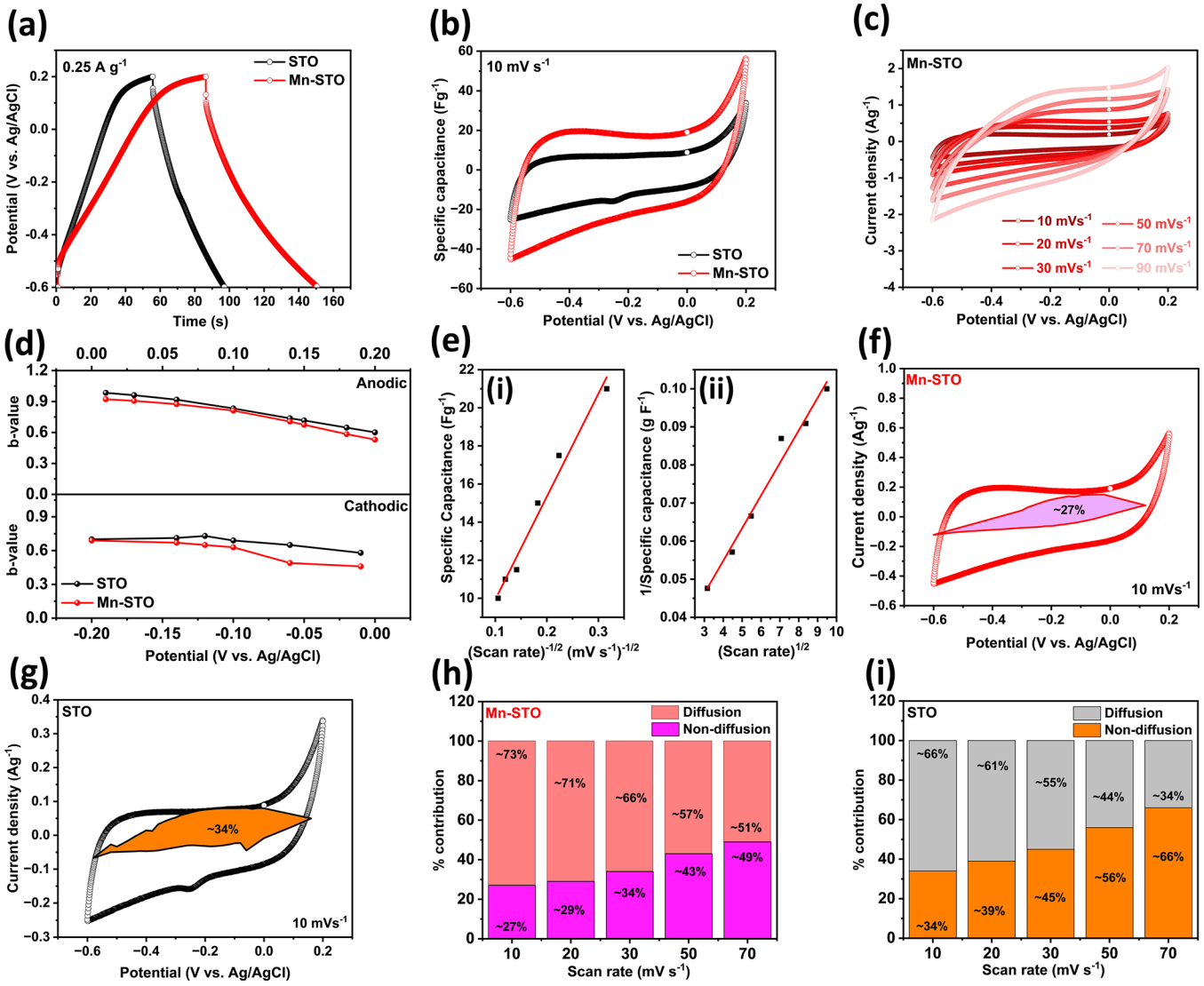

Figure 4. Comparison of (a) galvanostatic charge−discharge curve and (b) cyclic voltammogram of STO and Mn-STO in a half-cell configuration in an aqueous 3 M KOH electrolyte. (c) Cyclic voltammogram at different scan rates of the Mn-STO half-cell. (d) Anodic (upper panel) and cathodic (lower panel) *b*-values at different electrode potentials of STO and Mn-STO electrodes. (e) Plot showing the "specific capacitance" vs $v^{-1/2}$ (left panel) and "inverse of specific capacitance" vs $v^{1/2}$ (right panel) of Mn-STO electrodes used to calculate the surface charge storage and total charge storage by using Trasatti et al.'s method. The cyclic voltammogram at 10 mV s^{-1} differentiates the diffusion current contribution and nondiffusion current contribution (shaded region) of (f) Mn-STO and (g) STO electrodes. Histogram showing the diffusion and nondiffusion charge storage contribution (%) in (h) Mn-STO and (i) STO electrodes at different scan rates.

neutral electrolytes (Figure S6). This improved electrochemical performance in alkaline electrolytes can be attributed to the oxygen anion intercalation facilitated by the presence of OH^- ions in the electrolyte.[52] Further, the electrochemical performance of Mn-STO electrodes in the alkaline aqueous 3 M KOH electrolyte is analyzed by invoking the galvanostatic charge−discharge and cyclic voltammetry experiments in a three-electrode setup, where Ag/AgCl and platinum wire are the reference and counter electrodes, respectively, and is compared with that of the pristine STO electrodes. The charge−discharge curves and cyclic voltammograms, recorded within the potential window of −0.6 to 0.2 V vs Ag/AgCl, show a clear improvement in the Mn-STO electrodes compared to pristine STO (Figure 4a,b). This enhancement is attributed to the increased electrochemical surface area (Figure S5) and higher electronic conductivity, as evidenced by the lower band gap in Mn-STO (Figure 1e). Further, the quasi-rectangular shape of the cyclic voltammogram displayed by both STO and Mn-STO electrodes indicates the presence of both diffusion- and nondiffusion-controlled ion storage kinetic processes that can be evaluated from the cyclic voltammogram taken at different scan rates (Figure 4c and Figure S7).[53−56] The qualitative analysis of diffusion- and nondiffusion-controlled ionic kinetics can be evaluated from the *b*-value by utilizing the power law.[57−59]

$$i = av^b \tag{1}$$

where i is the dependent current as a function of sweep rate, v is the sweep rate, and a and b are the adjustable parameters. The lower anodic and cathodic *b*-values at different potentials in Mn-STO compared to STO (Figure 4d), estimated from the linear fitting of $\log(i)$ vs $\log(v)$ (Figure S8), show the prominent diffusion-controlled ion transfer process in Mn-STO due to the high bulk nonsurface-controlled pseudocapa-

https://doi.org/10.1021/acsomega.4c08911
ACS Omega 2024, 9, 47332−47341

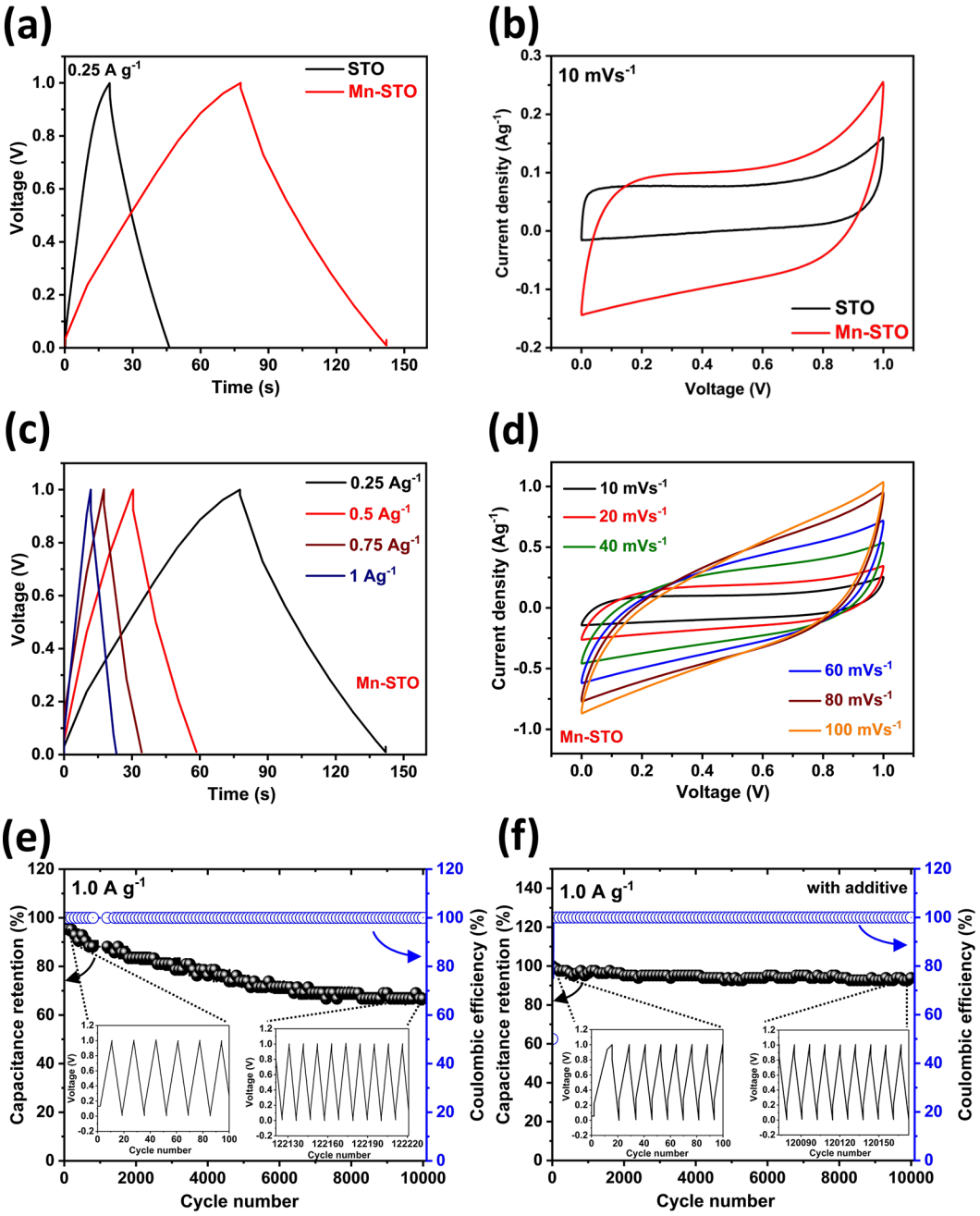

Figure 5. Comparison of (a) galvanostatic charge−discharge curve at a current density of 0.25 A g^{-1} and (b) cyclic voltammogram at a scan rate of 10 mV s^{-1} of STO and Mn-STO symmetric cells in a 3 M KOH aqueous electrolyte. (c) Galvanostatic charge−discharge at different current densities and (d) cyclic voltammogram at different scan rates of the symmetric Mn-STO supercapacitor. Cycling stability measurement of the Mn-STO symmetric supercapacitor at a current density of 1 A g^{-1} (e) without adding an additive and (f) with a 0.1 M $MnSO_4$ electrolyte additive in an aqueous 3 M KOH electrolyte up to 10,000 cycles.

citive nature.[60,61] This can be further empirically verified by Trasatti et al.'s method,[59,62,63] with an assumption that the total charge stored is contributed by the surface capacitive and bulk volume components. The surface and bulk ion-storage contributions can be differentiated from the surface ion storage and total ion storage calculated by extrapolating the sweep rate to infinity and zero, respectively, in the "specific capacitance" vs $v^{-1/2}$ (Figure 4e, left panel, and Figure S9a) and the "1/specific capacitance" vs $v^{1/2}$ plots (Figure 4e, right panel, and Figure S9b).[59,64] The ion-storage calculation from Trasatti et al.'s method shows that the bulk ion storage is ∼4% higher in Mn-STO (∼90% of the total capacitance) than in pristine STO (∼86% of the total capacitance).

The diffusion- and nondiffusion-controlled processes can be further evaluated quantitatively by making the assumption that the total current at every potential is contributed by the nondiffusion "k_1v" and diffusion "$k_2v^{1/2}$" current.[57,65−67]

$$i(V) = k_1v + k_2v^{0.5} \tag{2}$$

By rearranging, we get

$$\frac{i(V)}{v^{0.5}} = k_1v^{0.5} + k_2v \tag{3}$$

https://doi.org/10.1021/acsomega.4c08911
ACS Omega 2024, 9, 47332−47341

where k_1 and k_2 are the nondiffusion and diffusion current coefficients, estimated from the "slope" and "y-intercept", respectively, of the linear plot (Figure S10a−d) generated from Figure 4. The analysis further showed the increased diffusion-controlled storage process in Mn-STO with only ∼27% (shaded area, Figure 4f) nondiffusion contribution compared to STO, which shows ∼34% (shaded area, Figure 4g) nondiffusion current contribution at a scan rate of 10 mV s^{-1}. The histogram displays the quantitative differentiation of diffusion- and nondiffusion-controlled processes in Mn-STO (Figure 4h) and STO (Figure 4i), respectively, indicating an increase in the nondiffusion processes with scan rates. However, overall, in all scan rates, the diffusion process is predominant in Mn-STO than in STO. This again shows the reason for the increased bulk pseudocapacitive nature in Mn-STO than in STO, which can be attributed to the increased defects that occur in Mn-STO that can provide more sites to $-OH/O_2$ species, which can contribute higher oxygen anion diffusion storage along with cation storage.

A symmetrical supercapacitor using Mn-STO and STO materials was fabricated in a 3 M KOH alkaline electrolyte, and its electrochemical performance was evaluated through galvanostatic charge−discharge and cyclic voltammetry measurements within a voltage window of 0−1 V. The high charge/discharge time in the voltage profile (Figure 5a) and the large geometrical area of the cyclic voltammogram (Figure 5b) demonstrate that the Mn-STO symmetric cell delivers superior electrochemical performance compared to the STO symmetric cell. Further, the specific capacity ($C_{sc\_cd} = 2 \times I_g \times \Delta t$, C g^{-1}) and average specific capacitance ($C_{sc\_cv} = \frac{2I_g}{\upsilon}$, F g^{-1}) at the current density (I_g) of 0.25 A g^{-1} and the scan rate (υ) of 10 mV s^{-1} show an approximately 2-fold rise in Mn-STO (C_{sc_cd} = ∼ 32.5 C g^{-1} and C_{sc_cv} = ∼15.5 F g^{-1}) than the pristine STO (C_{sc_cd} = ∼18 C g^{-1} and C_{sc_cv} = ∼8 F g^{-1}) symmetric cell.[68−70] At higher current densities (Figure 5c and Figure S11a) and scan rates (Figure 5d, S11b), the specific capacity (Figure S12a) and average specific capacitance (Figure S12b) of the Mn-STO cells are found to be decreasing fast compared to those of pristine STO, which is due to the high diffusion-controlled storage processes in Mn-STO material. Moreover, the stability studies at a current density of 1 A g^{-1} show that Mn-STO undergoes capacitive degradation and retains only ∼67% of the initial capacitance (Figure 5e). This large capacitance degradation is due to the presence of Mn^{3+} in the crystal lattice of STO in Mn-doped STO, which is evident from the XPS data (Figure 3d), which undergoes a Jahn−Teller effect and is disproportionated into Mn^{4+} and Mn^{2+} ions. The formed Mn^{2+} ions are dissolved in the strong alkali electrolytes (3 M KOH), forming bonds with the OH^--coordinated complex and creating $Mn(OH)_2$ compounds, leading to large capacitance degradation.[71−73] Utilizing a Mn^{2+} additive in the aqueous electrolyte is one of the methods to suppress the Mn^{2+} dissolution, which suppresses the migration of Mn^{2+} from the electrode to the electrolyte.[74−77] Thus, the use of an alkaline aqueous 3 M KOH electrolyte with 0.1 M $MnSO_4$ results in improved cyclability, where the Mn-STO symmetric supercapacitor retains 100% initial capacitance even after 10,000 cycles with 100% Coulombic efficiency (Figure 5f), and the device stability is again ensured from the negligible change in the electrochemical impedance spectra taken before and after the cycling stability test (Figure S13). In short, the Mn-STO materials show a better pseudocapacitive electrochemical performance than pristine STO, which can be a potential electrode material for supercapacitor devices in suitable electrolytes.

4. CONCLUSIONS

This work reveals, for the first time, the anion storage capability of Mn-doped STO compared with pristine STO. The solid-state synthesized materials exhibit a pure cubic crystalline structure that remains unaltered by Mn doping. Different characterization techniques, such as XRD, EDAX, XPS, and EPR, confirm the successful partial substitution (∼4%) of Mn^{4+} for Ti^{4+} in the STO crystal lattice, reducing the UV−Vis optical band gap from ∼3.2 eV in pristine STO to ∼2.5 eV in Mn-STO. Additionally, the synthesized Mn-STO material shows the presence of Mn^{3+} and defective sites capable of adsorbing more OH^-/O_2 species, thereby exhibiting enhanced electronic conductivity and a 3-fold increase in electrochemical surface area. The half-cell electrochemical tests in 3 M KOH show Mn-STO electrodes outperforming pristine STO, with ∼73% of the process being diffusion-controlled compared to ∼66% for pristine STO at a scan rate of 10 mV s^{-1}. This indicates enhanced pseudocapacitive anion storage in Mn-STO due to increased defect sites from doping. Furthermore, the symmetric supercapacitor fabricated with Mn-STO exhibited ∼1.8 times higher specific capacitance than the pristine STO supercapacitor. Moreover, the cycling stability of the Mn-STO supercapacitor is improved with 0.1 M $MnSO_4$ electrolyte additives, achieving 100% capacitance retention after 10,000 cycles. This study investigates the pseudocapacitive anion storage properties of Mn-doped STO material in alkaline aqueous electrolytes, highlighting its potential application in electrochemical supercapacitors. Moreover, the increased diffusion-controlled process for anion insertion after Mn doping in STO may be a common characteristic of metal-doped perovskites. To support this hypothesis, further fundamental research comparing cation and anion storage in both undoped and metal-doped perovskites is needed.

■ ASSOCIATED CONTENT

Supporting Information

The Supporting Information is available free of charge at https://pubs.acs.org/doi/10.1021/acsomega.4c08911.

Rietveld refinement of STO and Mn-STO and their structural parameters, calculation of Goldschmidt tolerance factor, EDAX spectrum and elemental mapping of STO and Mn-STO, atomic percentage from EDAX, XPS survey scan and binding energy of STO and Mn-STO, electrochemical surface area (ECSA) calculation, cyclic voltammograms for ECSA calculation, calculation of b-values, diffusion and nondiffusion contribution, and galvanostatic charge−discharge, cyclic voltammetry, and electrochemical impedance spectroscopy analysis (PDF)

■ AUTHOR INFORMATION

Corresponding Authors

Susanta S. Roy − *Department of Physics, School of Natural Science, Shiv Nadar Institution of Eminence, Gautam Buddha Nagar, Uttar Pradesh 201314, India*;
Email: susanta.roy@snu.edu.in

https://doi.org/10.1021/acsomega.4c08911
ACS Omega 2024, 9, 47332−47341

Binson Babu − *Department of Physics, School of Natural Science, Shiv Nadar Institution of Eminence, Gautam Buddha Nagar, Uttar Pradesh 201314, India;* orcid.org/0000-0002-4275-2740; Email: binson.babu@snu.edu.in

Author

Dushyant K. Sharma − *Department of Physics, School of Natural Science, Shiv Nadar Institution of Eminence, Gautam Buddha Nagar, Uttar Pradesh 201314, India*

Complete contact information is available at: https://pubs.acs.org/10.1021/acsomega.4c08911

Notes

The authors declare no competing financial interest.

■ ACKNOWLEDGMENTS

D. K. Sharma is grateful to Shiv Nadar Institution of Eminence for providing a Ph.D. scholarship, instrumental facilities, and research funding. We acknowledge FIST Project Sanction Number SR/FST/PS-I/2017/6(C) for support of the Raman measurements. We are also grateful to the Department of Chemistry of Shiv Nadar Institution of Eminence for providing the EPR facility JEOL Model No. X320, X band.

■ REFERENCES

(1) Mefford, J. T.; Hardin, W. G.; Dai, S.; Johnston, K. P.; Stevenson, K. J. Anion Charge Storage through Oxygen Intercalation in LaMnO3 Perovskite Pseudocapacitor Electrodes. *Nat. Mater.* **2014**, *13* (7), 726−732.

(2) Che, W.; Wei, M.; Sang, Z.; Ou, Y.; Liu, Y.; Liu, J. Perovskite LaNiO3-δ Oxide as an Anion-Intercalated Pseudocapacitor Electrode. *J. Alloys Compd.* **2018**, *731*, 381−388.

(3) Cao, X.-L.; Ren, T.-Z.; Yuan, Z.-Y.; Bandosz, T. J. CaTiO3 Perovskite in the Framework of Activated Carbon and Its Effect on Enhanced Electrochemical Capacitance. *Electrochim. Acta* **2018**, *268*, 73−81.

(4) Huang, J.; Hu, L.; Yang, Z.; Li, J.; Wang, P.; Wei, Y.; Sun, P. Hollow Spherical LaFeO3 Perovskite as Anode Material for Lithium-Ion Battery. *Inorg. Chem. Commun.* **2023**, *150*, No. 110458.

(5) Zhang, C.; Zhang, Y.; Nie, Z.; Wu, C.; Gao, T.; Yang, N.; Yu, Y.; Cui, Y.; Gao, Y.; Liu, W. Double Perovskite La2MnNiO6 as a High-Performance Anode for Lithium-Ion Batteries. *Advanced Science* **2023**, *10* (18), No. 2300506.

(6) Weng, G.-M.; Kong, J.; Wang, H.; Karpovich, C.; Lipton, J.; Antonio, F.; Fishman, Z. S.; Wang, H.; Yuan, W.; Taylor, A. D. A Highly Efficient Perovskite Photovoltaic-Aqueous Li/Na-Ion Battery System. *Energy Storage Materials* **2020**, *24*, 557−564.

(7) Cao, Y.; Liang, J.; Li, X.; Yue, L.; Liu, Q.; Lu, S.; Asiri, A. M.; Hu, J.; Luo, Y.; Sun, X. Recent Advances in Perovskite Oxides as Electrode Materials for Supercapacitors. *Chem. Commun.* **2021**, *57* (19), 2343−2355.

(8) Ahangari, M.; Mostafaei, J.; Sayyah, A.; Mahmoudi, E.; Asghari, E.; Coruh, A.; Delibas, N.; Niaei, A. Investigation of Structural and Electrochemical Properties of SrFexCo1-xO3-δ Perovskite Oxides as a Supercapacitor Electrode Material. *Journal of Energy Storage* **2023**, *63*, No. 107034.

(9) Wilde, P. M.; Guther, T. J.; Oesten, R.; Garche, J. Strontium Ruthenate Perovskite as the Active Material for supercapacitors1Dedicated to Professor W. Vielstich on the Occasion of His 75th Birthday.1. *J. Electroanal. Chem.* **1999**, *461* (1), 154−160.

(10) Kudo, T.; Obayashi, H.; Gejo, T. Electrochemical Behavior of the Perovskite-Type Nd1 − x Srx CoO3 in an Aqueous Alkaline Solution. *J. Electrochem. Soc.* **1975**, *122* (2), 159.

(11) Wattiaux, A.; Fournès, L.; Demourgues, A.; Bernaben, N.; Grenier, J. C.; Pouchard, M. A Novel Preparation Method of the SrFeO3 Cubic Perovskite by Electrochemical Means. *Solid State Commun.* **1991**, *77* (7), 489−493.

(12) Mahesh, R.; Kannan, K. R.; Rao, C. N. R. Electrochemical Synthesis of Ferromagnetic LaMnO3 and Metallic NdNiO3. *J. Solid State Chem.* **1995**, *114* (1), 294−296.

(13) Wohlfahrt-Mehrens, M.; Schenk, J.; Wilde, P. M.; Abdelmula, E.; Axmann, P.; Garche, J. New Materials for Supercapacitors. *J. Power Sources* **2002**, *105* (2), 182−188.

(14) Grenier, J.-C.; Pouchard, M.; Wattiaux, A. Electrochemical Synthesis: Oxygen Intercalation. *Curr. Opin. Solid State Mater. Sci.* **1996**, *1* (2), 233−240.

(15) Piovano, A.; Agostini, G.; Frenkel, A. I.; Bertier, T.; Prestipino, C.; Ceretti, M.; Paulus, W.; Lamberti, C. Time Resolved in Situ XAFS Study of the Electrochemical Oxygen Intercalation in SrFeO2.5 Brownmillerite Structure: Comparison with the Homologous SrCoO2.5 System. *J. Phys. Chem. C* **2011**, *115* (4), 1311−1322.

(16) Karvonen, L.; Valkeapää, M.; Liu, R.-S.; Chen, J.-M.; Yamauchi, H.; Karppinen, M. O-K and Co-L XANES Study on Oxygen Intercalation in Perovskite SrCoO3-δ. *Chem. Mater.* **2010**, *22* (1), 70−76.

(17) Shao, T.; You, H.; Zhai, Z.; Liu, T.; Li, M.; Zhang, L. Hollow Spherical LaNiO3 Supercapacitor Electrode Synthesized by a Facile Template-Free Method. *Mater. Lett.* **2017**, *201*, 122−124.

(18) Zhu, L.; Liu, Y.; Su, C.; Zhou, W.; Liu, M.; Shao, Z. Perovskite SrCo0.9Nb0.1O3− as an Anion-Intercalated Electrode Material for Supercapacitors with Ultrahigh Volumetric Energy Density. *Angew. Chem., Int. Ed.* **2016**, *55* (33), 9576−9579.

(19) Deshmukh, V. V.; Ravikumar, C. R.; Kumar, M. R. A.; Ghotekar, S.; Kumar, A. N.; Jahagirdar, A. A.; Murthy, H. C. A. Structure, Morphology and Electrochemical Properties of SrTiO3 Perovskite: Photocatalytic and Supercapacitor Applications. *Environmental Chemistry and Ecotoxicology* **2021**, *3*, 241−248.

(20) Cao, Y.; He, H.; Li, S.; Ruan, P.; Yi, J.; Qiu, W. The Preparation and Modification of Strontium Titanate Ceramic Films for High-Performance Flexible Supercapacitor. *ChemElectroChem.* **2023**, *10* (5), No. e202200947.

(21) Sopiha, K. V.; Malyi, O. I.; Persson, C.; Wu, P. Band Gap Modulation of SrTiO3 upon CO2 Adsorption. *Phys. Chem. Chem. Phys.* **2017**, *19* (25), 16629−16637.

(22) Sharma, D. K.; Sain, S.; Maity, G.; Thomas, A.; Kumar, R.; Dhar, S.; Arora, H. S.; Babu, B.; Roy, S. S. Electrochemical Studies on Chromium Doped SrTiO3 for Supercapacitor Applications. *Nano Trends* **2024**, *6*, No. 100036.

(23) Chen, H.-C.; Huang, C.-W.; Wu, J. C. S.; Lin, S.-T. Theoretical Investigation of the Metal-Doped SrTiO3 Photocatalysts for Water Splitting. *J. Phys. Chem. C* **2012**, *116* (14), 7897−7903.

(24) Sun, H.; Dong, C.; Huang, A.; Zhan, H.; Wang, G.; Liu, W.; Ma, B.; Wang, W. Transition Metal Doping Induces Ti3+ to Promote the Performance of SrTiO3@TiO2 Visible Light Photocatalytic Reduction of CO2 to Prepare C1 Product. *Chem. - Eur. J.* **2022**, *28* (28), No. e202200019.

(25) Priyadharsini, C. I.; Marimuthu, G.; Pazhanivel, T.; Anbarasan, P. M.; Aroulmoji, V.; Prabhu, S.; Ramesh, R. Electrochemical Supercapacitor Studies of Ni2+-Doped SrTiO3 Nanoparticles by a Ball Milling Method. *Ionics* **2020**, *26* (7), 3591−3597.

(26) Shannon, R. D. Revised Effective Ionic Radii and Systematic Studies of Interatomic Distances in Halides and Chalcogenides. *Acta Crystallogr., Sect. A* **1976**, *32* (5), 751−767.

(27) Wu, G.; Li, P.; Xu, D.; Luo, B.; Hong, Y.; Shi, W.; Liu, C. Hydrothermal Synthesis and Visible-Light-Driven Photocatalytic Degradation for Tetracycline of Mn-Doped SrTiO3 Nanocubes. *Appl. Surf. Sci.* **2015**, *333*, 39−47.

(28) Trepakov, V.; Makarova, M.; Stupakov, O.; Tereshina, E. A.; Drahokoupil, J.; Čerňanský, M.; Potůček, Z.; Borodavka, F.; Valvoda, V.; Lynnyk, A.; Jäger, A.; Jastrabik, L.; Dejneka, A. Synthesis, Structure and Properties of Heavily Mn-Doped Perovskite-Type SrTiO3 Nanoparticles. *Mater. Chem. Phys.* **2014**, *143* (2), 570−577.

(29) Yang, H.; Kan, K.; Ouyang, J.; Li, Y. Solvothermal Synthesis and Optical Properties of Mn2+-Doped SrTiO3 Powders. *J. Alloys Compd.* **2009**, *485* (1), 351−355.
(30) Neacsu, C. C.; Dreyer, J.; Behr, N.; Raschke, M. B. Scanning-Probe Raman Spectroscopy with Single-Molecule Sensitivity. *Phys. Rev. B* **2006**, *73* (19), No. 193406.
(31) Rout, D.; Moon, K.-S.; Kang, S.-J. L.; Kim, I. W. Dielectric and Raman Scattering Studies of Phase Transitions in the (100−x)Na0.5Bi0.5TiO3−xSrTiO3 System. *J. Appl. Phys.* **2010**, *108* (8), No. 084102.
(32) Dugu, S.; Pavunny, S. P.; Sharma, Y.; Scott, J. F.; Katiyar, R. S. Disorder Driven Structural and Dielectric Properties of Silicon Substituted Strontium Titanate. *J. Appl. Phys.* **2015**, *118* (3), No. 034105.
(33) Rabuffetti, F. A.; Kim, H.-S.; Enterkin, J. A.; Wang, Y.; Lanier, C. H.; Marks, L. D.; Poeppelmeier, K. R.; Stair, P. C. Synthesis-Dependent First-Order Raman Scattering in SrTiO3 Nanocubes at Room Temperature. *Chem. Mater.* **2008**, *20* (17), 5628−5635.
(34) Schaufele, R. F.; Weber, M. J. First- and Second-Order Raman Scattering of SrTiO3. *J. Chem. Phys.* **1967**, *46* (7), 2859−2861.
(35) Nilsen, W. G.; Skinner, J. G. Raman Spectrum of Strontium Titanate. *J. Chem. Phys.* **1968**, *48* (5), 2240−2248.
(36) Ma, P. P.; Liu, X. Q.; Zhang, F. Q.; Xing, J. J.; Chen, X. M. Sr(Ga0.5Nb0.5)1−xTixO3 Low-Loss Microwave Dielectric Ceramics with Medium Dielectric Constant. *J. Am. Ceram. Soc.* **2015**, *98* (8), 2534−2540.
(37) Hadj Youssef, A.; Zhang, J.; Ehteshami, A.; Kolhatkar, G.; Dab, C.; Berthomieu, D.; Merlen, A.; Légaré, F.; Ruediger, A. Symmetry-Forbidden-Mode Detection in SrTiO3 Nanoislands with Tip-Enhanced Raman Spectroscopy. *J. Phys. Chem. C* **2021**, *125* (11), 6200−6208.
(38) Dias, A.; Moreira, R. L. Crystal Structure and Phonon Modes of Ilmenite-Type NaBiO3 Investigated by Raman and Infrared Spectroscopies. *J. Raman Spectrosc.* **2010**, *41* (6), 698−701.
(39) Pokorný, J.; Pasha, U. M.; Ben, L.; Thakur, O. P.; Sinclair, D. C.; Reaney, I. M. Use of Raman Spectroscopy to Determine the Site Occupancy of Dopants in BaTiO3. *J. Appl. Phys.* **2011**, *109* (11), No. 114110.
(40) Levin, I.; Cockayne, E.; Lufaso, M. W.; Woicik, J. C.; Maslar, J. E. Local Structures and Raman Spectra in the Ca(Zr,Ti)O3 Perovskite Solid Solutions. *Chem. Mater.* **2006**, *18* (3), 854−860.
(41) Liu, X.; Fang, B.; Deng, J.; Yan, H.; Deng, H.; Yue, Q.; Ding, J.; Zhao, X.; Luo, H. Study of Temperature-Dependent Raman Spectroscopy and Electrical Properties in [001]-Oriented 0.35Pb(In1/2Nb1/2)O3−0.35Pb(Mg1/3Nb2/3)O3−0.30PbTiO3-Mn Single Crystals. *J. Appl. Phys.* **2016**, *119* (1), No. 014105.
(42) Ouillon, R.; Pinan-Lucarre, J. P.; Ranson, P.; Pruzan, P.; Mishra, S. K.; Ranjan, R.; Pandey, D. A Raman Scattering Study of the Phase Transitions in SrTiO3 and in the Mixed System (Sr1-xCax)TiO3 at Ambient Pressure from T = 300 K down to 8 K. *J. Phys.: Condens. Matter* **2002**, *14* (8), 2079.
(43) Mylsamy, S.; Karazhanov, S.; Subramanian, B. Lattice Distortion-Driven Band Gap Engineering and Enhanced Electrocatalytic Activity of Mn-Substituted Nanostructured SrTiO3Materials: A Comprehensive Investigation. *Chemosphere* **2024**, *346*, No. 140577.
(44) Choudhury, D.; Pal, B.; Sharma, A.; Bhat, S. V.; Sarma, D. D. Magnetization in Electron- and Mn- Doped SrTiO3. *Sci. Rep.* **2013**, *3* (1), 1433.
(45) Mansoor, H.; Harrigan, W. L.; Lehuta, K. A.; Kittilstved, K. R. Reversible Control of the Mn Oxidation State in SrTiO3 Bulk Powders. *Front. Chem.* **2019**, *7*, No. 353.
(46) Müller, K. A. Electron Paramagnetic Resonance of Manganese IV in SrTi\mathrmO_3. *Phys. Rev. Lett.* **1959**, *2* (8), 341−343.
(47) Zorko, A.; Pregelj, M.; Luetkens, H.; Axelsson, A.-K.; Valant, M. Intrinsic Paramagnetism and Aggregation of Manganese Dopants in SrTiO_3. *Phys. Rev. B* **2014**, *89* (9), No. 094418.
(48) Wong, C. P. P.; Lai, C. W.; Lee, K. M.; Pan, G. T.; Huang, C. M.; Juan, J. C.; Yang, T. C. K. Enhancement of Discharge Capacity and Energy Density by Oxygen Vacancies in Nickel Doped SrTiO3 as Cathode for Rechargeable Alkaline Zinc Battery. *Electrochim. Acta* **2022**, *404*, No. 139705.
(49) Wu, Y.; He, T. Ag Loading Induced Visible Light Photocatalytic Activity for Pervoskite SrTiO3 Nanofibers. *Spectrochimica Acta Part A: Molecular and Biomolecular Spectroscopy* **2018**, *199*, 283−289.
(50) Pan, X.; Shuai, Y.; Wu, C.; Luo, W.; Sun, X.; Zeng, H.; Bai, X.; Gong, C.; Jian, K.; Zhang, L.; Guo, H.; Tian, B.; Zhang, W. Switchable Diode Effect in Oxygen Vacancy-Modulated SrTiO3 Single Crystal. *Appl. Phys. A: Mater. Sci. Process.* **2017**, *123* (9), 574.
(51) Bard, A. J.; Faulkner, L. R. *Electrochemical Methods: Fundamentals and Applications*; 2nd ed.; John Wiley & Sons: New York, 2001.
(52) Liu, Y.; Dinh, J.; Tade, M. O.; Shao, Z. Design of Perovskite Oxides as Anion-Intercalation-Type Electrodes for Supercapacitors: Cation Leaching Effect. *ACS Appl. Mater. Interfaces* **2016**, *8* (36), 23774−23783.
(53) Liu, J.; Wang, J.; Xu, C.; Jiang, H.; Li, C.; Zhang, L.; Lin, J.; Shen, Z. X. Advanced Energy Storage Devices: Basic Principles, Analytical Methods, and Rational Materials Design. *Adv. Sci.* **2018**, *5* (1), No. 1700322.
(54) Babu, B.; Simon, P.; Balducci, A. Fast Charging Materials for High Power Applications. *Adv. Energy Mater.* **2020**, *10* (29), No. 2001128.
(55) Elgrishi, N.; Rountree, K. J.; McCarthy, B. D.; Rountree, E. S.; Eisenhart, T. T.; Dempsey, J. L. A Practical Beginner's Guide to Cyclic Voltammetry. *J. Chem. Educ.* **2018**, *95* (2), 197−206.
(56) Pholauyphon, W.; Charoen-amornkitt, P.; Suzuki, T.; Tsushima, S. Perspectives on Accurately Analyzing Cyclic Voltammograms for Surface- and Diffusion-Controlled Contributions. *Electrochem. Commun.* **2024**, *159*, No. 107654.
(57) Sathiya, M.; Prakash, A. S.; Ramesha, K.; Tarascon, J.; Shukla, A. K. V2O5-Anchored Carbon Nanotubes for Enhanced Electrochemical Energy Storage. *J. Am. Chem. Soc.* **2011**, *133* (40), 16291−16299.
(58) Babu, B.; Shaijumon, M. M. Studies on Kinetics and Diffusion Characteristics of Lithium Ions in TiNb2O7. *Electrochim. Acta* **2020**, *345*, No. 136208.
(59) Babu, B.; Shaijumon, M. M. High Performance Sodium-Ion Hybrid Capacitor Based on Na2Ti2O4(OH)2 Nanostructures. *J. Power Sources* **2017**, *353*, 85−94.
(60) Augustyn, V.; Come, J.; Lowe, M. A.; Kim, J. W.; Taberna, P.-L.; Tolbert, S. H.; Abruña, H. D.; Simon, P.; Dunn, B. High-Rate Electrochemical Energy Storage through Li+ Intercalation Pseudocapacitance. *Nat. Mater.* **2013**, *12* (6), 518−522.
(61) Wang, J.; Polleux, J.; Lim, J.; Dunn, B. Pseudocapacitive Contributions to Electrochemical Energy Storage in TiO2 (Anatase) Nanoparticles. *J. Phys. Chem. C* **2007**, *111* (40), 14925−14931.
(62) Ardizzone, S.; Fregonara, G.; Trasatti, S. Inner" and "Outer" Active Surface of RuO2 Electrodes. *Electrochim. Acta* **1990**, *35* (1), 263−267.
(63) Baronetto, D.; Krstajić, N.; Trasatti, S. Reply to "Note on a Method to Interrelate Inner and Outer Electrode Areas" by H. *Vogt. Electrochim. Acta* **1994**, *39* (16), 2359−2362.
(64) Huang, C.; Zhang, J.; Young, N. P.; Snaith, H. J.; Grant, P. S. Solid-State Supercapacitors with Rationally Designed Heterogeneous Electrodes Fabricated by Large Area Spray Processing for Wearable Energy Storage Applications. *Sci. Rep.* **2016**, *6* (1), 25684.
(65) Babu, B.; Shaijumon, M. M. Understanding How Degree of Crystallinity Affects Electrochemical Kinetics of Sodium-Ion in Brown TiO2 Nanotubes. *ChemElectroChem.* **2021**, *8* (12), 2180−2185.
(66) Babu, B.; Ullattil, S. G.; Prasannachandran, R.; Kavil, J.; Periyat, P.; Shaijumon, M. M. Ti3+ Induced Brown TiO2 Nanotubes for High Performance Sodium-Ion Hybrid Capacitors. *ACS Sustainable Chem. Eng.* **2018**, *6* (4), 5401−5412.
(67) Bhat, S. S. M.; Babu, B.; Feygenson, M.; Neuefeind, J. C.; Shaijumon, M. M. Nanostructured Na2Ti9O19 for Hybrid Sodium-Ion Capacitors with Excellent Rate Capability. *ACS Appl. Mater. Interfaces* **2018**, *10* (1), 437−447.

https://doi.org/10.1021/acsomega.4c08911
ACS Omega 2024, 9, 47332−47341

(68) Laheäär, A.; Przygocki, P.; Abbas, Q.; Béguin, F. Appropriate Methods for Evaluating the Efficiency and Capacitive Behavior of Different Types of Supercapacitors. *Electrochem. Commun.* **2015**, *60*, 21−25.
(69) Brousse, T.; Bélanger, D.; Long, J. W. To Be or Not to Be Pseudocapacitive? *J. Electrochem. Soc.* **2015**, *162* (5), A5185−A5189.
(70) Damien, D.; Babu, B.; Narayanan, T. N.; Reddy, A. L.; Ajayan, P. M.; Shaijumon, M. M. Eco-Efficient Synthesis of Graphene Nanoribbons and Its Application in Electrochemical Supercapacitors. *Graphene* **2013**, *1* (1), 37−44.
(71) Shin, J.; Seo, J. K.; Yaylian, R.; Huang, A.; Meng, Y. S. A Review on Mechanistic Understanding of MnO2 in Aqueous Electrolyte for Electrical Energy Storage Systems. *International Materials Reviews* **2020**, *65* (6), 356−387.
(72) Dai, L.; Wang, Y.; Sun, L.; Ding, Y.; Yao, Y.; Yao, L.; Drewett, N. E.; Zhang, W.; Tang, J.; Zheng, W. Jahn−Teller Distortion Induced Mn2+-Rich Cathode Enables Optimal Flexible Aqueous High-Voltage Zn-Mn Batteries. *Advanced Science* **2021**, *8* (12), No. 2004995.
(73) Tran, T. N. T.; Jin, S.; Cuisinier, M.; Adams, B. D.; Ivey, D. G. Reaction Mechanisms for Electrolytic Manganese Dioxide in Rechargeable Aqueous Zinc-Ion Batteries. *Sci. Rep.* **2021**, *11* (1), 20777.
(74) Herrmann, N. J.; Euchner, H.; Groß, A.; Horstmann, B. The Cycling Mechanism of Manganese-Oxide Cathodes in Zinc Batteries: A Theory-Based Approach. *Adv. Energy Mater.* **2024**, *14* (1), No. 2302553.
(75) Kim, S. H.; Oh, S. M. Degradation Mechanism of Layered MnO2 Cathodes in Zn/ZnSO4/MnO2 Rechargeable Cells. *J. Power Sources* **1998**, *72* (2), 150−158.
(76) Chamoun, M.; Brant, W. R.; Tai, C.-W.; Karlsson, G.; Noréus, D. Rechargeability of Aqueous Sulfate Zn/MnO2 Batteries Enhanced by Accessible Mn2+ Ions. *Energy Storage Materials* **2018**, *15*, 351−360.
(77) Chen, H.; Dai, C.; Xiao, F.; Yang, Q.; Cai, S.; Xu, M.; Fan, H. J.; Bao, S.-J. Reunderstanding the Reaction Mechanism of Aqueous Zn−Mn Batteries with Sulfate Electrolytes: Role of the Zinc Sulfate Hydroxide. *Adv. Mater.* **2022**, *34* (15), No. 2109092.

https://doi.org/10.1021/acsomega.4c08911
ACS Omega 2024, 9, 47332−47341